Research Article

The mechanical performance of cementless total knee replacements: it's not all about the maximum loads†

MECHANICAL PERFORMANCE OF CEMENTLESS TKR

Fernando J Quevedo González[1], Joseph D Lipman[1], Darrick Lo[1], Ivan De Martino[1], Peter K Sculco[1], Thomas P Sculco[1], Fabio Catani[2], Timothy Wright[1]

[1] Hospital for Special Surgery, New York, NY, USA

[2] University of Modena, Modena, Italy

Corresponding author

Fernando J Quevedo González

Hospital for Special Surgery, 535 East 71st Street, New York, NY 10021

quevedogonzalezf@hss.edu

Phone: (646) 797-8276

†This article has been accepted for publication and undergone full peer review but has not been through the copyediting, typesetting, pagination and proofreading process, which may lead to differences between this version and the Version of Record. Please cite this article as doi: [10.1002/jor.24194]

Received 08 August 2018; Revised 11 November 2018; Accepted 13 November 2018

Journal of Orthopaedic Research®

DOI 10.1002/jor.24194

Author contributions

All authors have read and approved the final submitted manuscript

Fernando J Quevedo González: study design, finite element simulations, data analysis and interpretation and manuscript preparation

Joseph D Lipman: Study design, data interpretation and manuscript revision

Darrick Lo: Study design, data interpretation and manuscript revision

Ivan De Martino: Study design, virtual implantation, data interpretation and manuscript revision

Peter K Sculco: Study design, virtual implantation, data interpretation and manuscript revision

Thomas P Sculco: Study design, virtual implantation, data interpretation and manuscript revision

Fabio Catani: kinematic data collection, virtual implantation, study design, data interpretation and manuscript revision

Timothy Wright: Study design, data interpretation and manuscript revision

Abstract

Finite element (FE) models are frequently used to assess mechanical interactions between orthopaedic implants and surrounding bone. However, FE studies are often limited by: the small number of bones that are modeled; the use of normal bones that do not reflect the altered bone density distributions that result from osteoarthritis (OA); and the application of simplified load cases usually based on peak forces and without consideration of tibiofemoral kinematics. To overcome these limitations, we undertook an integrated approach to determine the most critical scenario for the interaction between an uncemented tibial component and surrounding proximal tibial bone. A cementless component, based on a modern design, was virtually implanted using computed-tomography scans from 13 patients with knee OA. FE simulations were performed across a demanding activity, stair ascent, by combining in vivo experimental forces from the literature with tibiofemoral kinematics measured from patients who had received the same design of knee component. The worst conditions for the bone-implant interaction, in terms of micromotion and percentage of interfacial bone mass at risk of failure, did not arise from the maximum applied loads. We also found large variability among bones and tibiofemoral kinematics sets. Our results suggest that future FE studies should not focus solely on peak loads as this approach does not consistently correlate to worst-case scenarios. Moreover, multiple load cases and multiple bones should be considered to best reflect variations in tibiofemoral kinematics, anatomy, and tissue properties. This article is protected by copyright. All rights reserved

Keywords: finite element, micromotion, bone failure, cementless tibia

Introduction

Component fixation in total knee replacement (TKR) continues to be a challenge, as aseptic loosening accounts for 20% to 40% of all TKR revisions[1 - 3]. While cemented implants continue to remain the gold standard, the use of cementless components is increasing thanks to newly highly porous ingrowth materials with potential to improve long term results. For cementless fixation, achieving long term survivorship requires bone ingrowth and mineralization into the porous surfaces of the implant components, thus securing a stable link between implant and bone. In order to achieve reliable osseous ingrowth, the relative micromotion between implant and bone must be low (< 20 - 50 μm[4, 5]). In addition, the implant must continuously transfer loads to the adjacent bone to minimize stress shielding but also must not overload the bone tissue, which could lead to osseous collapse and failure of the fixation.

Implant fixation is governed, therefore, in large part by the biomechanics of the bone-implant system, and as such researchers have applied finite element (FE) analyses to evaluate the risk of bone failure[6 - 8], implant migration[9], load transfer[10 - 13], bone resorption[14], and/or interfacial micromotions[11, 15 - 20]. While such analyses provide important insights, they are often limited by only modeling a few, usually normal (i.e., without underlying pathology), bones and a few, usually maximum, loading conditions that generally do not incorporate the tibiofemoral kinematics. Only Galloway et al.[7] simulated a large number of bones throughout an activity cycle; however, the condition of the bones (i.e., healthy or arthritic) was unknown and the loads were directly applied to the tibial tray, assuming even force distribution and static contact areas. Nonetheless, previous studies have shown that the biomechanical bone-implant interaction is influenced by bone-to-bone variability[6 - 8] and changes in bone modulus distribution that occur due to osteoarthritis (OA)[6]. In addition, it has been shown that peak micromotions can arise for

sub-maximal loads[15, 16, 18]. On the other hand, loads are often applied at the center of the condyles[6, 11] or distributed to the tibial plateau[7, 15, 18], yet Chong et al.[16] and Bartel et al.[21] showed that the location where the loads are applied to the tibial tray can markedly affect the load transfer to bone and micromotion between the implant and the bone.

To address these limitations, we undertook a comprehensive evaluation of the mechanical burden of a cementless tibial baseplate using an integrated approach in which multiple osteoarthritic bones were simulated across a demanding activity of daily living, stair ascent, accounting for experimentally measured tibiofemoral kinematics and loads (Fig. 1). Our aim was to determine 1) which instant of the activity cycle generated the most critical conditions for micromotion and risk of bone failure and 2) what was the variability in micromotion and risk of bone failure introduced by different bones and tibiofemoral kinematics.

Materials and methods

In a separate study, tibiofemoral kinematics were experimentally measured by fluoroscopy during stair ascent in 8 patients (6 females - 2 males, 61- 82 years old, BMI from 24 to 39 kg/m^2) who had undergone unilateral cemented TKR using the Physica Knee PS (Posterior Stabilized) design (LimaCorporate, Villanova di San Daniele, Udine, Italy). The anterior-posterior (AP) contact location on the medial and lateral condyles and the internal-external rotation between the femur and tibia were acquired every 5° and from 10° to 80° of knee flexion (Fig. 2).

Thirteen other patients with end stage OA about to undergo TKR underwent pre-operative CT scans as standard of care. All were female, from 58 – 80 years of age, with body mass indices (BMIs) ranging from 22 to 36 kg/m^2 and all with Kellgren-Lawrence grade 3 or 4 OA. One knee presented bi-compartmental OA, two knees presented lateral OA, and 10 knees present medial

OA. All CT scans were performed in the same center with the same scanning parameters (402 kVp and 135 mA). The 3D geometry of the proximal tibiae was reconstructed from the CT scans and virtual resection was performed perpendicular to the mechanical axis in the coronal plane and with 3 degrees of posterior slope in the sagittal plane. Each tibia was then virtually implanted with a Physica PS modular tibial component, under the guidance of fellowship trained orthopaedic surgeons (TPS, PKS, FC, IDM). The implant's AP midline was oriented with the medial third of the tibial tubercle, and the proper implant size was chosen to maximize coverage while avoiding overhang on the cut tibial surface. To mimic modern cementless knee implants, the fixation geometry of the implant was modified to two hexagonal pegs located posterior to the implant's medial-lateral (ML) midline (Fig. 3).

The tibial component and the bone were meshed with linear tetrahedral elements in Abaqus 2017 (Dassault Systemes, Providence, RI). The element size used for the bone increased from 1 mm at the proximal tibial cut to 2.5 mm at 40 mm distal to the tibial cut and to 3 mm at the distal fixed end of the tibia (77 mm distal to the resection). For the tibial component, the element size was 1mm except for the articular surfaces, where the size was decreased to 0.75 mm to allow for the proper definition of the load application according to the tibiofemoral kinematics. The resulting 13 models had between 486,532 and 960,622 linear elements.

The component materials were modeled as linear, isotropic, and homogeneous. Similar to modern cementless knee implants, the pegs and the inferior layer on the backside of the metallic tray were assumed to be LimaCorporate's 3D printed porous Trabecular Titanium^{TM} (TT), with an elastic modulus (E) of 1.1 GPa and a Poisson's ratio (υ) of 0.3. The remainder of the tibial tray was assumed to be Ti6Al4V (E=114.3 GPa, υ =0.33), while polyethylene (E=687 MPa, υ

=0.3) was considered for the tibial insert. The tibial insert and tibial tray were assumed to be rigidly bonded together.

The bone was modeled as a linear, isotropic, non-homogeneous material. The elastic modulus was assumed to be dependent on the apparent density, which was linearly related to the Hounsfield Units (HU) from the CT scans. Since the bones were not scanned alongside reference phantoms, we assumed that the 13-bone average minimum HU (-174.5) corresponded to an apparent density of 0 g/cm^3, and the 13-bone average maximum Hounsfield Units (1731) corresponded to a density of 1.8 g/cc[23]. The apparent density was then converted to elastic modulus by combining the empirical relationships from Morgan et al.[24] and Snyder and Schneider[25], which have been shown to adequately predict bone failure under daily activities and to correlate well with experimental data[23, 26]. To determine the loading profile for each of the 13 FE models, we relied on the experimental measurements from Bergmann et al.[22] (available online at http://orthoload.com), which consist of three net joint forces and three net joint moments, obtained as the average of in vivo measurements in 8 patients with telemeterized total knee replacements during stair ascent. The loading profiles were discretized into 26 loading steps (Fig. 4-a), and the magnitudes of the forces and moments were scaled to each of the 13 models based on the individual weights of the 13 patients who had been CT scanned. A single activity cycle was simulated, in which the loads and moments were applied to the load summation point situated at the center of the tibial baseplate, at the lowest point of the polyethylene insert[22]. At each loading instant, the tibiofemoral contact points were determined based on the knee flexion. All nodes on the articular surfaces within 10 mm of the contact points were kinematically coupled to the load summation point (Fig. 4-b). In all cases, the bones were fixed 77 mm distal to the proximal resection.

Finite element simulations were performed in Abaqus 2017 (Dassault Systemes), considering the bone-implant interface as frictional to represent the immediate post-operative scenario where no bone ingrowth has yet occurred. The friction coefficient between bone and TT was set to 1.1. This data was provided by LimaCorporate. In total, 104 cases were simulated, resulting from the combinations of each of the 13 tibiae with the eight different kinematics sets. To obtain the micromotion at the bone-implant interface, the closest node in the bone interface to each implant interfacial node was first determined in the original (i.e., unloaded) state. Then, the bone-implant interfacial micromotion was obtained as the difference in displacement between each pair of nodes. The risk of bone failure at the bone-implant interface was computed based on a principal strain failure criterion[24]. This assumes failure if the maximum tensile strain is larger than 7300 με or the minimum compressive strain is smaller than -6500 με.

Results

The maximum micromotion, considering the average of eight kinematics sets for each tibia, was computed at 72% of the stair ascent cycle (Fig. 5a). This was approximately double than that computed for the maximum applied load during the activity cycle (~ 35%). For most of the tibiae, the maximum micromotion was between 27 μm and 38 μm. However, one tibia (T-7 in Fig. 5a) generated a maximum of 20 μm, while tibiae T-3 and T-5 yielded maximum micromotions of 50 μm and 82 μm, respectively. Patient T-5 required the smallest implant size but had the third heaviest weight. Nevertheless, across the entire group, the maximum micromotion was only moderately correlated with the ratio of patient weight to implant coverage (R^2=0.35) and BMI (R^2=0.34).

In the most critical case for each tibia, the maximum micromotion arose at the anterior-lateral edge of the tibial tray (Fig. 6). Between 57% and 97% of the tray interface had micromotion smaller than 20 μm, below the most restrictive threshold for a stable interface[4]. Conversely, for the most critical case, a maximum of 21% of the interface had micromotions >50 μm, which can be considered the most generous threshold for a stable interface[5].

The largest percentage of interfacial bone mass at risk of failure (i.e., with strains larger than the yield strain of bone), considering the average of eight kinematics sets for each tibia, occurred at 72% of the cycle in all cases and was at least 1.5 times larger than the point in the cycle (~ 35%) when the maximum applied load occurred (Fig. 5b). The maximum percentage of interfacial bone mass at risk of failure was small in all cases (<0.6% of the bone-tibial tray interfacial mass) and was not correlated with BMI (R^2=0.15) or the ratio of patient's weight to implant coverage (R^2=0.05).

For 11 of the 13 tibiae, the bone at risk of failure in the most critical case was located at the posterior aspect of the lateral compartment of the bone-implant interface (Fig. 7). For tibiae T-4 and T-7, the bone at risk of failure was located in the posterior aspect of the medial tibia. Only T-5 showed failure at the implant's ML midline. The percentage of interfacial bone mass at risk of failure accumulated throughout the cycle was also computed. This was done by considering at each bone element the highest strain throughout the cycle. In general, the percentage of interfacial bone mass at risk of failure accumulated throughout the cycle was similar to the one obtained in the most critical scenario; however, tibiae T-1, T-4, T-7, and T-13 showed noticeable differences between both values (Fig. 8).

For each tibia, the variation in micromotion and percentage of interfacial bone mass at risk of failure introduced by multiple kinematic sets was computed as the range of values across the eight kinematics sets. Similarly, the variability introduced by multiple tibiae was computed, for each kinematic set, as the range across the 13 tibiae. For both, micromotion (Fig. 9a) and percentage of interfacial bone mass at risk of failure (Fig. 9b), the variation introduced by considering multiple tibiae was more important than the variation due to the eight kinematics sets.

Discussion

We sought to determine the most critical loading conditions during stair ascent for the interaction between a cementless tibial component for total knee replacement and the surrounding bone. This was done across multiple tibiae and included tibiofemoral kinematics to determine load location. We used micromotion at the bone-implant interface and the risk of bone failure at the interface as our measures of successful cementless fixation.

We found that the maximum micromotion and the maximum percentage of interfacial bone at risk of failure did not occur at point in the stair ascent cycle when the largest load was applied (~ 35% of the cycle), but instead at 72% of the cycle. This point in the cycle corresponds to the contralateral foot strike and is characterized by close-to-maximum axial and AP shear forces, maximum flexion-extension moment, and close-to-maximum internal-external and varus-valgus moments. Similarly, other authors have found the most critical micromotions to arise for sub-maximal loads[15, 16, 18]. Furthermore, we found that for some tibiae the percentage of interfacial bone mass at risk of failure in the most critical load case was smaller than the one accumulated throughout the cycle. Regardless of the particular instant of the activity cycle that yielded the

most critical conditions for the bone-implant interaction, these results show that single load cases, even when based on peak loads, can underestimate the burden placed on the bone-implant system.

We also found that the different tibiae and tibiofemoral kinematics sets introduced variability in the FE results. The variability was more important across tibiae than across kinematics sets and more important for micromotion than for the percentage of interfacial bone mass at risk of failure. The tibia that yielded the largest micromotion had the largest BMI; however, the values of micromotion and percentage of interfacial bone mass at risk of failure were only moderately correlated with the patient's BMI or the ratio of patient's weight to implant coverage. As an example, T-4 and T-9 both had BMI of 26; however, they yielded a maximum micromotion of 51μm and 37 μm, respectively. These results show the importance of considering multiple tibiae in the FE simulations of bone-implant interaction in order to capture the worst-case scenario. Moreover, they suggest that patient-specific simulations may play a relevant role when it comes to evaluating the suitability of an individual for cementless total knee replacement, as also previously suggested by Wong et al.[8]. In addition, the variability introduced by the tibiofemoral kinematics shows that the location where loads are applied affects the FE results. Therefore, as previously suggested[16], the tibiofemoral kinematics should be considered for the application of loads, as opposed to centered on the articular surfaces[6, 10] or distributed to the tibial tray[7, 15, 18].

Our study has limitations. First, the results were not experimentally validated. Direct validation of the FE results was impossible because the input data for the models corresponded to living subjects. Nevertheless, the maximum micromotion values that we computed (20-82 μm) are within the range of values found in previous studies[16, 18]. On the other hand, Tuncer et al.[26] demonstrated that the density to modulus relationships considered here adequately predict the

bone surface strains, upon which the risk of bone failure was based. Second, we did not include muscle forces. However, the forces and moments that we considered, reported by Bergmann et al.,[22] correspond to the loads generated by the femur on the tibia under the loading environment that include the loads contributed by the ground reaction, gravity (body weight), inertia, and muscles. Therefore, including the muscle forces would not have impacted the results at the bone-implant interface. Finally, the alignment of the implant in the FE models was not the same as during the in-vivo measurements of tibiofemoral loads or kinematics. In addition, we considered a particular implant design, posterior stabilized, and a particular fixation technique, cementless fixation. In this way, we applied the joint loads measured by Bergmann et al.[22] to the FE models, and we assumed that they were the same across tibiofemoral kinematic sets. Nonetheless, differences in component alignment and implant's articular design will alter the kinematics, and consequently, the loads at the joint. Moreover, the variables of interest for other component fixation methods (i.e., cement) will be different. However, these potential changes do not reduce the validity of the main conclusion of our work, that the bone-implant interaction may be underestimated when considering single loads based on peak forces. Finally, the patient CT scans did not include reference phantoms, creating uncertainty in the Hounsfield Unit to density relationship; however, we followed an approach reported in previous studies[23] that included experimental validation of FE results [26].

In conclusion, we integrated multiple osteoarthritic bones, experimentally measured forces and tibiofemoral kinematics into a series of FE models of cementless TKR implants. Our results support evaluating the bone-implant interaction for multiple bones and for a variety of loading conditions, including changes in tibiofemoral kinematics to ensure the worst-case scenario is captured. Furthermore, the lack of correlation between micromotion and patient-based

parameters suggest that patient-specific models may be useful tools to evaluate the suitability of a patient for cementless total knee replacement.

Conflict of interest

This study was funded by a research contract with LimaCorporate (Villanova di San Daniele, Udine, Italy) under a research contract. Ivan De Martino, Peter K Sculco, and Thomas P Sculco are consultants for LimaCorporate.

Acknowledgements

The authors thank Dr. Giorgio Franceschi for his help with the CT scan data and patient demographics.

References

[1] Thiele K, Perka C, Matziolis G, et al. 2015. Current Failure Mechanisms After Knee Arthroplasty Have Changed: Polyethylene Wear Is Less Common in Revision Surgery. J Bone Joint Surg Am 97(9): 715-720.

[2] Sharkey PF, Lichstein PM, Shen C, et al. 2014. Why are total knee arthroplasties failing today - has anything changed after 10 years? J Arthroplasty 29(9): 1774-1778.

[3] Pitta M, Esposito CI, Li Z, et al. 2018. Failure after modern total knee arthroplasty: a prospective study of 18,065 knees. J Arthroplasty 33(2): 407-414.

[4] Jasty M, Bragdon C, Burke D, et al. 1997. In vivo skeletal responses to porous-surfaced implants subjected to small induced motions. J Bone Joint Surg Am 79(5): 707-714.

[5] Jasty M, Bragdon C, Zalenski E, et al. 1997. Enhanced stability of uncemented canine femoral components by bone ingrowth into the porous coatings. J Arthroplasty 12(1): 106-113.

[6] Perillo-Marcone A, Ryd L, Johnsson K, Taylor M. 2004. A combined RSA and FE study of the implanted proximal tibia: correlation of the post-operative mechanical environment with implant migration. J Biomech 37(8): 1205-1213.

[7] Galloway F, Kahnt M, Ramm H, et al. 2013. A large scale finite element study of a cementless osseointegrated tibial tray. J Biomech 46(11): 1900-1906.

[8] Wong J, Steklov N, Patil S, et al. 2011. Predicting the effect of tray malalignment on risk for bone damage and implant subsidence after total knee arthroplasty. J Orthop Res 29(3): 347-353.

[9] Taylor M, Tanner K, Freeman MR. 1998. Finite element analysis of the implanted proximal tibia: a relationship between the initial cancellous bone stresses and implant migration. J Biomech 31(4): 303-310.

[10] Completo A, Talaia P, Fonseca F, Simões JA. 2009. Relationship of design features of stemmed tibial knee prosthesis with stress shielding and end-of-stem pain. Mat Des 30(4): 1391-1397.

[11] Rakotomanana LR, Leyvraz PF, Curnier A, et al. 1994. Comparison of tibial fixations in total knee arthroplasty: an evaluation of stress distribution and interface micromotions. The Knee 1(2): 91-99.

[12] Au AG, Liggins AB, Raso VJ, Amirfazli A. 2005. A parametric analysis of fixation post shape in tibial knee prostheses. Med Eng Phys 27(2): 123-134.

[13] Rawlinson JJ, Peters LE, Campbell DA, et al. 2005. Cancellous bone strains indicate efficacy of stem augmentation in constrained condylar knees. Clin Orthop Relat Res 440: 107-116.

[14] Chong DY, Hansen UN, van der Venne R, et al. 2011. The influence of tibial component fixation techniques on resorption of supporting bone stock after total knee replacement. J Biomech 44(5): 948-954.

[15] Taylor M, Barret DS, Deffenbaugh D. 2012. Influence of loading and activity on the primary stability of cementless tibial trays. J Orthop Res 30(9): 1362-1368.

[16] Chong DY, Hansen UN, Amis AA. 2010. Analysis of bone-prosthesis interface micromotion for cementless tibial prosthesis fixation and the influence of loading conditions. J Biomech 43(6): 1074-1080.

[17] Hashemi A, Shirazi-Adl A. 2000. Finite element analysis of tibial implants - effect of fixation design and friction model. Comput Methods Biomech Biomed Engin 3(3): 183-201.

[18] Fitzpatrick CK, Hemelaar P, Taylor M. 2014. Computationally efficient prediction of bone-implant interface micromotion of a cementless tibial tray during gait. J Biomech 47(7): 1718-1726.

[19] Barker DS, Tanner KE, Ryd L. 2005. A circumferentially flanged tibial tray minimizes bone-tray shear micromotion. Proc Inst Mech Eng [H] J Eng Med 219(6): 449-456.

[20] Keja M, Wevers HW, Siu D, Grootenboer H. 1994. Relative motion at the bone-prosthesis interface. Clin Biomech 9(5): 275-283.

[21] Bartel DL, Burstein AH, Santavicca EA, Insall JN. 1982. Performance of the tibial component in total knee replacement. J Bone Joint Surg Am 64(7): 1026-1033.

[22] Bergmann G, Bender A, Graichen F, et al. 2014. Standardized loads acting in knee implants. PLoS One 9(1): e86035.

[23] Tuncer M, Hansen UN, Amis AA. 2014. Prediction of structural failure of tibial bone models under physiological loads: effect of CT density-modulus relationships. Med Eng Phys 36(8): 991-997.

[24] Morgan E, Bayraktar HH, Keaveny TM. 2003. Trabecular bone modulus-density relationships depend on anatomic site. J Biomech 36(7):897-904.

[25] Snyder SM, Schneider E. 1991. Estimation of mechanical properties of cortical bone by computed tomography. J OrthopRes 9(3): 422-431.

[26] Tuncer M, Cobb JP, Hansen UN, Amis AA. 2013. Validation of multiple subject-specific finite element models of unicompartmental knee replacement. Med Eng Phys 35(10): 1457-1464.

Figure legends

Figure 1 - Flowchart of the study

Figure 2 - Tibiofemoral kinematics during stair ascent from eight knee arthroplasty patients. Medial and lateral contact points determined fluoroscopically between 10° and 80° of flexion every 5°

Figure 3 - Implant design and materials considered in the simulations

Figure 4 – (a) Discretized knee flexion angle, resultant force, and moment. The loads correspond to the high values for a 100 kg patient[22] (average of 8 patients, from http://orthoload.com). (b) FE model of one of the tibiae, showing the tibiofemoral contact locations for a particular point in the cycle (in red) and the applied loads

Figure 5 – (a) Micromotion and (b) percentage of interfacial bone mass at risk of failure (i.e., with strain above yield strain of bone). Average of eight kinematics sets for each of the 13 tibiae (T-1 to T-13)

Figure 6 – Distribution of micromotion for each tibia for the most critical case (i.e., the one that yielded the largest micromotion)

Figure 7 – Distribution of the risk of bone failure at the tibia resection for the most critical scenario of each tibia. Values are shown as a percentage of the yield strain of bone (εYT=6500 $\mu\varepsilon$; εYC=-7300 $\mu\varepsilon$[24]). The bone at risk of failure is shown in black

Figure 8 - Comparison of the percentage of interfacial bone mass at risk of failure accumulated throughout the entire cycle and at the most critical case. The percentage of interfacial bone mass at risk of failure accumulated throughout the entire cycle was computed by considering the largest strain across the entire cycle at each bone element. The percentage of interfacial bone mass at risk of failure computed at the most critical case is the maximum value obtained throughout the cycle

Figure 9 – Boxplots of (a) maximum micromotion and (b) percentage of interfacial bone mass at risk of failure for each tibia. For each tibia, each point corresponds to the maximum value across the cycle for a tibiofemoral contact set

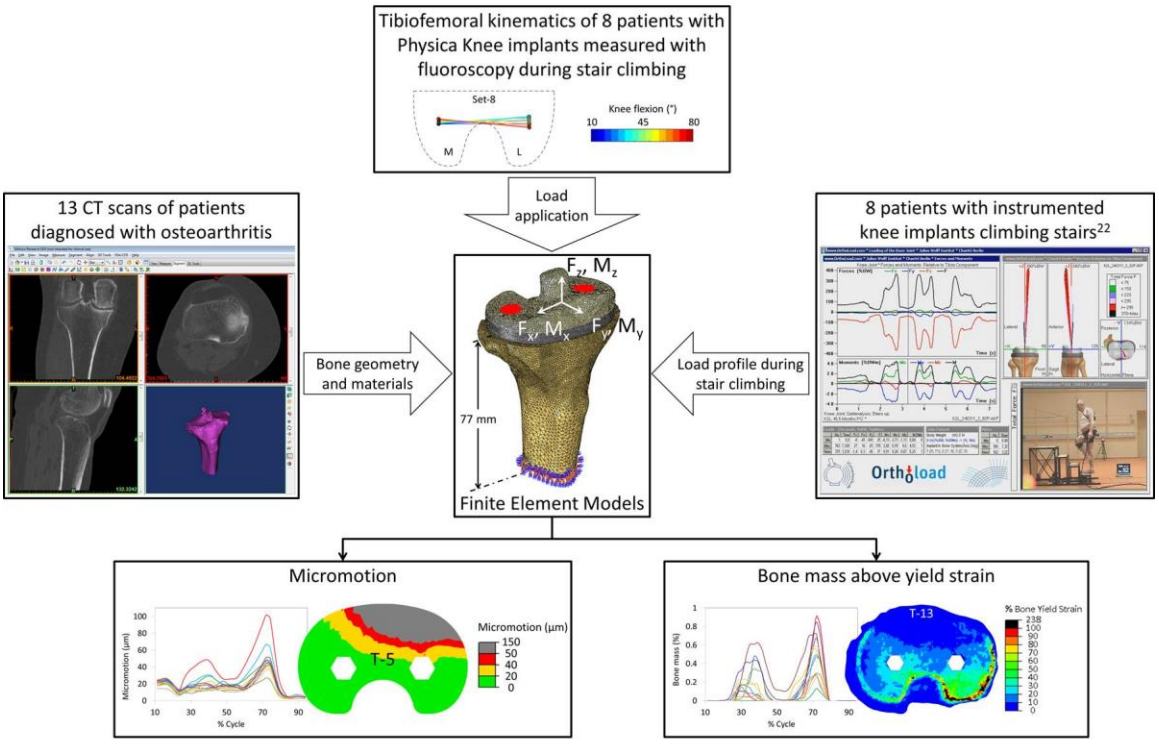

Figure 1

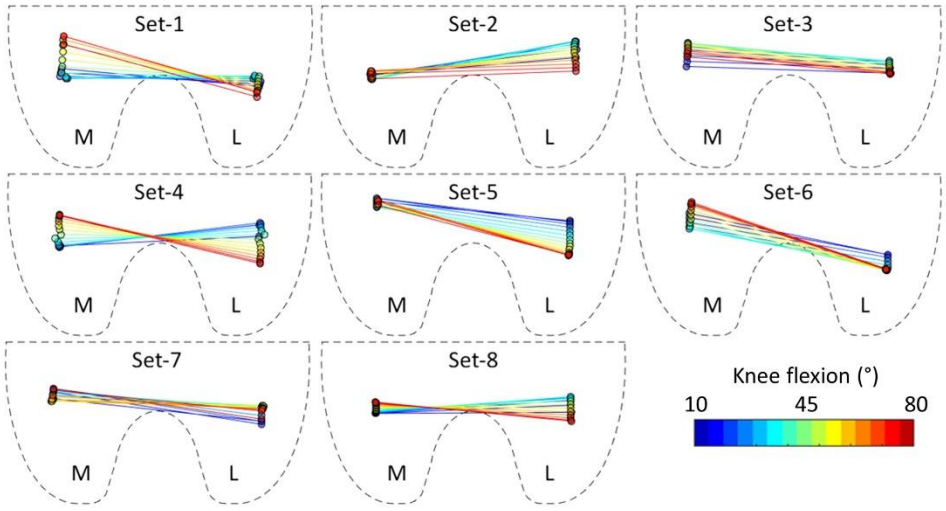

Figure 2

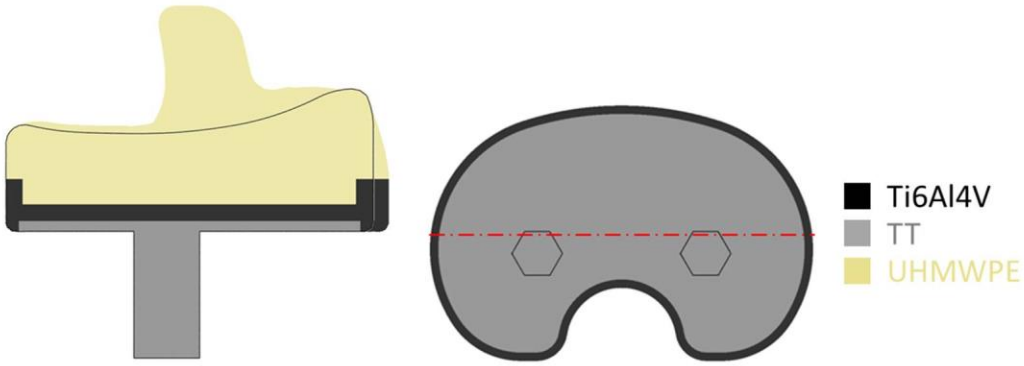

Figure 3

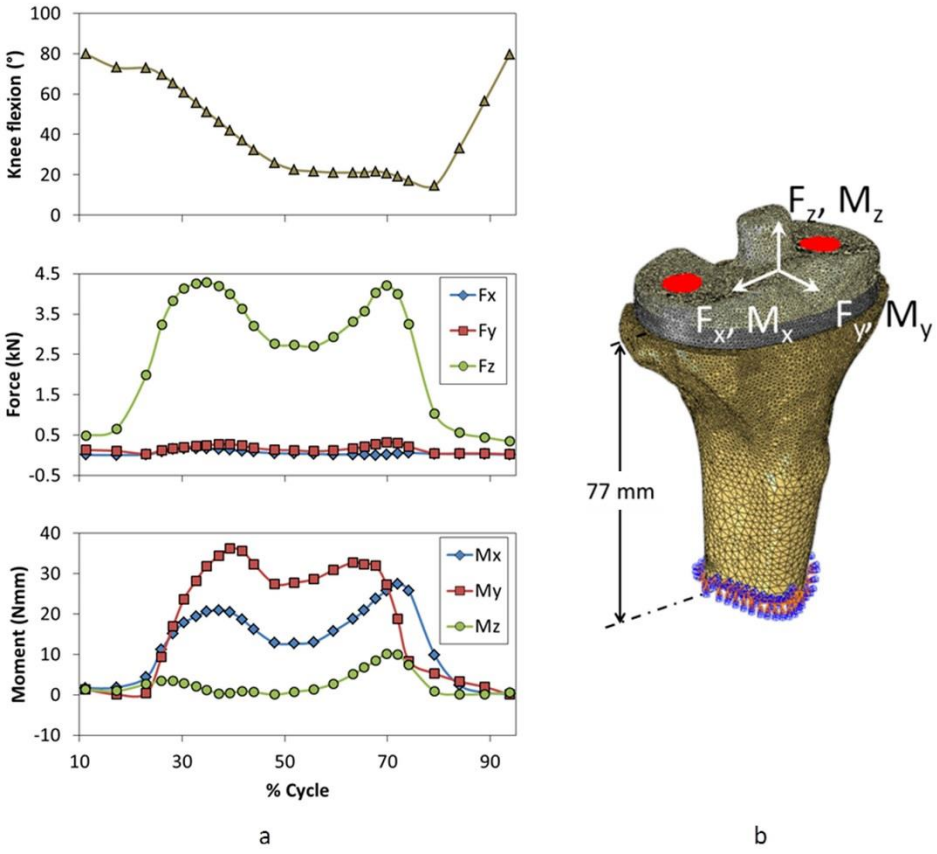

Figure 4

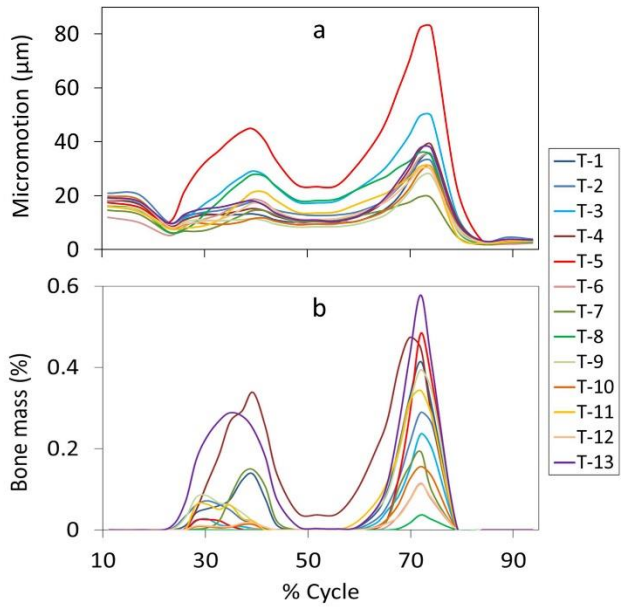

Figure 5

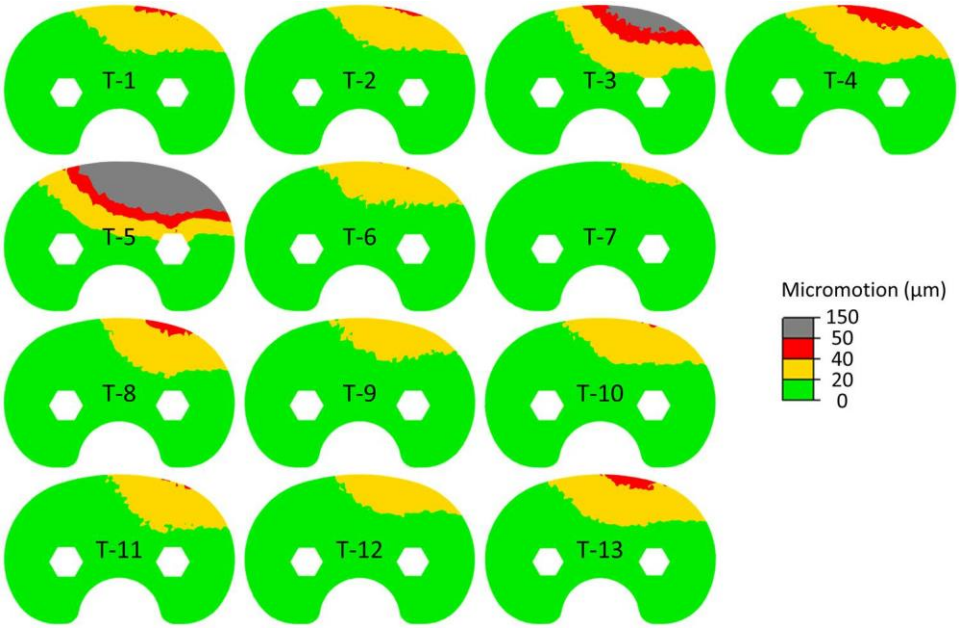

Figure 6

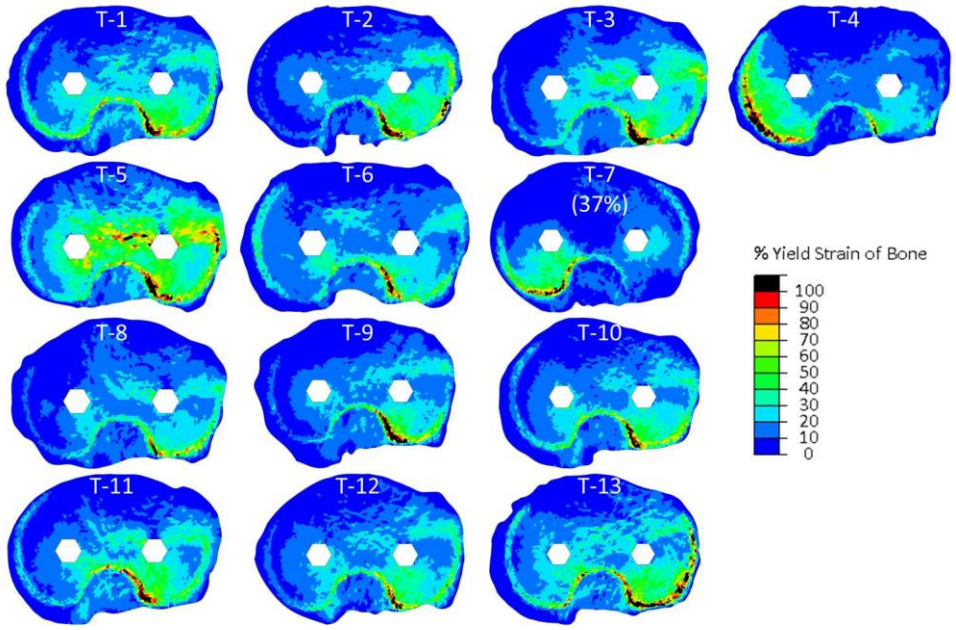

Figure 7

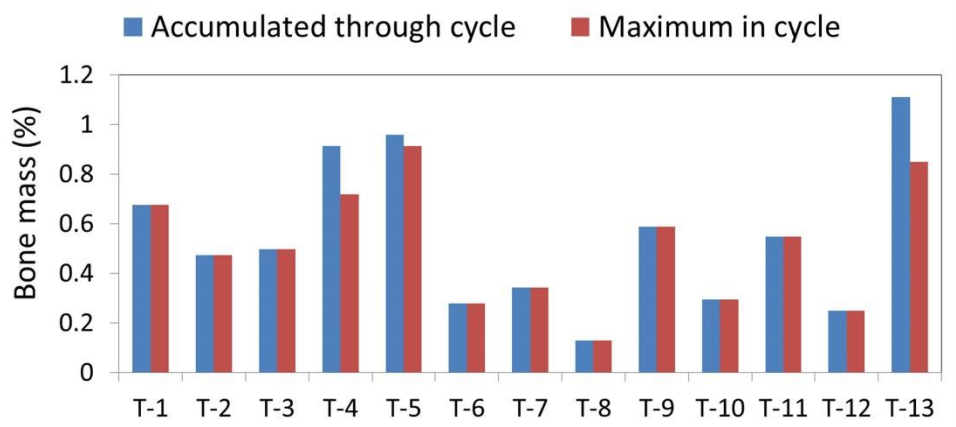

Figure 8

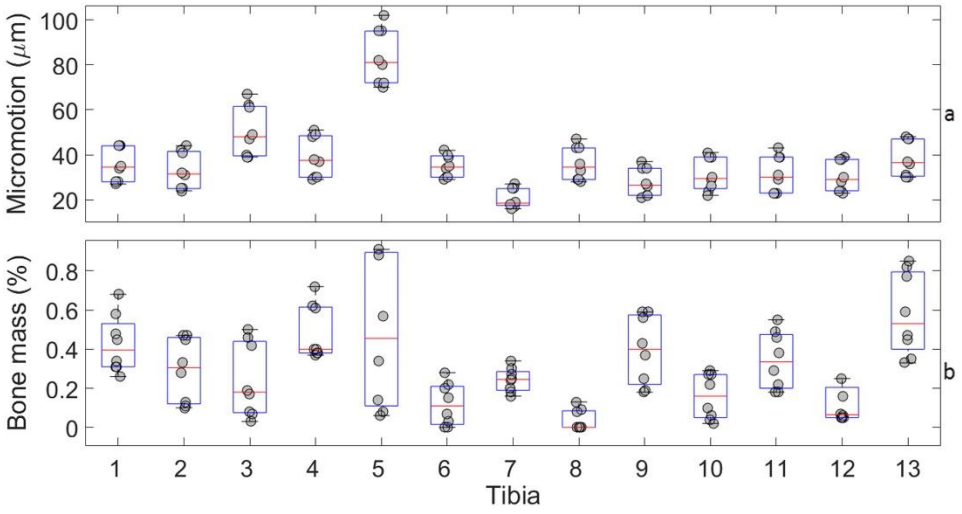

Figure 9